

# Shape from Projections via Differentiable Forward Projector for Computed Tomography

Jakeoung Koo<sup>a</sup>, Anders B. Dahl<sup>a</sup>, J. Andreas Bærentzen<sup>a</sup>, Qiongyang Chen<sup>b</sup>, Vedrana A. Dahl<sup>a</sup>

<sup>a</sup>Technical University of Denmark, Anker Engelds Vej 1, Kgs. Lyngby, 2800, Denmark

<sup>b</sup>University of Antwerp, Prinsstraat 13, Antwerpen, 2000, Belgium

## Abstract

In computed tomography, the reconstruction is typically obtained on a voxel grid. But in this work, we propose a mesh-based reconstruction method. For tomographic problems, 3D meshes have mostly been studied to simulate data acquisition, but not for reconstruction, which for a 3D mesh means the inverse process of estimating shapes from projections. In this paper, we propose a differentiable forward model for 3D meshes that bridge the gap between the forward model for 3D surfaces and optimization. We view the forward projection as a rendering process, and make it differentiable by extending recent work in differentiable rasterization. We use the proposed forward model to reconstruct 3D shapes directly from projections. Experimental results for single-object problems show that our method outperforms traditional voxel-based methods on noisy simulated data. We also apply our method on electron tomography images of nanoparticles to demonstrate the applicability of the method on real data.

## 1. Introduction

In computed tomography (CT), we aim at solving the inverse problem of computing the 3D structure (shape and attenuation) of an object from a set of projection images (Buzug, 2008) taken from different angles. Here, the geometry and the physics of the imaging system is known, which allows us to model the forward process, i.e. if we have a suggestion for the 3D structure of the imaged object, we can compute the projection images.

We need a data structure to represent the structure of the object that should be reconstructed. The most common data structure is a volumetric image, with voxel intensities representing local attenuation. This approach may be used for reconstructing any type of object. Since each voxel in the volume is a parameter that must be computed, we have a very large number of unknowns. This makes it difficult to reconstruct volumes in situations where we e.g. have projections from a limited angular view (e.g., in electron tomography) or noisy data, it can be difficult to accurately compute the attenuations in all voxels. Therefore, we propose to use a mesh to represent the shape of the object. The mesh separates the object into parts with a constant attenuation.

In tomography, forward projection of 3D meshes has mostly been used for simulating tomographic data acquisition, i.e. modeling the forward projection. This includes modeling X-ray transmission imaging based on Monte-Carlo methods (Bonin et al., 2002; Freud et al., 2006) or ray tracing techniques (Freud et al., 2006; Marinovszki et al., 2018). Furthermore, Vidal et al. (2009); Sujar et al. (2017) took the advantage of the OpenGL library to simulate X-ray images in real time. However, none of the proposed methods are concerned with reconstruction, i.e. solving the inverse problem.

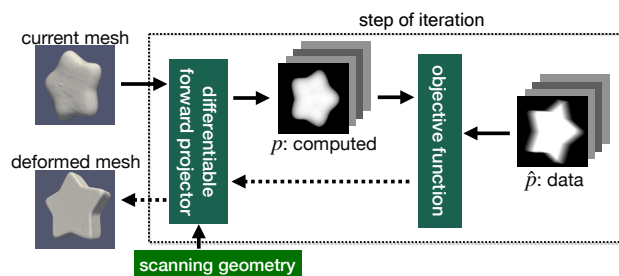


Figure 1: The proposed differentiable forward projector enables optimizing a 3D mesh from projections for computed tomography. Given a mesh and scanning geometry, the forward projector computes projections for the current mesh, which is updated by deforming vertices in the direction that minimizes our objective function.

For the mesh-based tomographic reconstruction that we propose, the reconstruction problem is two-fold. The mesh must be deformed to follow the boundaries of the depicted object, and in each part of the object, a single attenuation coefficient must be estimated. To forward project the mesh, we employ rendering techniques, which allow a very efficient projection of the 3D mesh to the detector plane. We extend the differentiable rasterizer recently proposed by Chen et al. (2019) to derive differentiable forward projection. This enables us to compute vertex displacements that deform the mesh based on the difference between the forward projection and projection data. In Fig. 1, we provide an overview of our shape estimation method. In Fig. 2, we illustrate how our work differs from existing image-based reconstruction methods (Andersen and Kak, 1984; Buzug, 2008).

Our model has been developed for problems like X-ray CT where the damping of the X-ray attenuation coefficient are modeled as linearly dependent on the path length through the sample (Buzug, 2008), which is also assumed in electron tomography (Aveyard et al., 2017) where coefficient is related to electron scattering (Midgley and Dunin-Borkowski, 2009).

\*Corresponding author: jakoo@dtu.dk

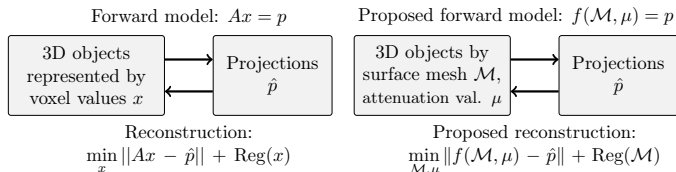


Figure 2: Algebraic reconstruction vs. our proposed approach. *Left*: Existing algebraic reconstruction methods use a linear system of equations to model the forward projections typically together with some regularization to constrain the solution. *Right*: We propose a differentiable forward model  $f$  which computes projections for an object represented by a triangular mesh and attenuation coefficients  $\mu$ . This forward model is used to reconstruct the shape from projections data  $\hat{p}$ .

In summary, our contribution is two-fold. We suggest a differentiable forward projector to generate projections from 3D meshes, and we propose a shape estimation method employing the differentiable forward projector. Our code is available online: <https://github.com/jakeoung/ShapeFromProjections>.

## 2. Related works

*Differentiable rendering based on rasterization.* In our work we deform a mesh by changing vertex positions using gradient descent. Therefore, we need the gradient of our objective function with respect to vertex coordinates, which is possible through differentiating the forward projection. As observed in (Vidal et al., 2009), the tomographic forward projection can be implemented by extending a rendering technique in computer graphics based on rasterization. Such rasterization-based rendering technique projects 3D models onto 2D image plane and involves a discrete step to choose the pixels covered by triangles of 3D models. This discrete step is not differentiable in conventional graphics pipelines. Making such rasterization-based rendering differentiable, called *differentiable rasterization*, has been studied by several works to connect rendering and optimization. As our work extends such differentiable rasterization techniques, we first review those works and explain the difference to our work.

The general framework OpenDR, that was proposed by Loper and Black (2014), approximated gradients of pixel values with respect to model parameters. Kato et al. (2018) suggested a heuristic forward and backward pass where blurring is used to avoid zero gradients. This approach has an inconsistency between the forward and backward pass, and to circumvent this inconsistency, Liu et al. (2019) proposed a method called SoftRas by relaxing discrete rasterization process into the aggregation of smooth probability functions. Unlike the conventional rasterization rendering, in SoftRas, each face in the mesh affects many pixels in the image plane, which is computationally costly and memory-demanding.

Chen et al. (2019) suggested an interpolation-based differentiable rasterizer called DIB-R. DIB-R reformulates the barycentric interpolation in the rasterization process to analytically derive the gradients. Our forward projector extends this reformulation when computing the thickness of an object for computed

tomography, but differs in some aspects. The rendering techniques such as DIB-R can improve the performance by ignoring invisible faces, but since we model penetrating radiation, our forward projector needs to consider all the faces. DIB-R used the idea of SoftRas (Liu et al., 2019) for background pixels to propagate the gradients on those background, but our forward projector does not use it to reduce the computational cost.

*Shape reconstruction from projections.* Our proposed method is related to tomographic segmentation, where segments are directly computed from projections. This includes (Elangovan and Whitaker, 2001; Whitaker and Elangovan, 2002; Alvino and Yezzi, 2004) that are based on the Mumford-Shah model (Mumford and Shah, 1989) where boundaries are represented using level-sets (Osher and Fedkiw, 2004). Recently, the parametric level-set method (Aghasi et al., 2011) has been used for tomographic segmentation in (Kadu et al., 2018; Eliasof et al., 2020) where level-sets are represented as an aggregation of radial basis functions. Although the parametric level-set method has fewer unknown variables, its forward projection still depends on a regular grid. Gadelha et al. (2019) uses a deep convolutional neural network for 2D tomographic reconstruction, where the forward projection is based on the transformation of a regular grid and resampling. On the other hand, the work (Dahl et al., 2018) based on snakes (Kass et al., 1988) avoids a dense grid – it represents curves explicitly and proposes a direct forward projection of the curves. However, this method is limited to a single 2D curve, while our method supports 3D objects. Another difference is that (Dahl et al., 2018) evolves curves in the normal directions of curve points, while our deformation can displace the vertices in all directions.

In summary, existing shape estimation methods from projections are either based on dense regular grid or limited to single 2D curve. To our knowledge, our work is the first to propose the differentiable forward projector for 3D triangular mesh and use it for reconstructing shapes from projections.

## 3. Differentiable forward projector

In this section, we describe our main contribution of the differentiable forward projector. The goal is to forward project triangular meshes and make this process differentiable with respect to 3D vertex positions and attenuation coefficients. This differentiable forward projection will be used for optimizing the mesh shape described in Sec. 4. First we describe the case of a single object and then extend to composite objects.

### 3.1. Single object

Consider an object represented by a watertight triangle mesh. The object is homogeneous, i.e. it has a certain attenuation coefficient  $\mu$  associated with the volume inside the mesh. For now, we consider  $\mu$  constant, we will later explain how it is computed. The mesh consists of  $K$  vertices, and we write  $\mathbf{v}_k$  for the 3D coordinates of the vertex  $k$ .

To simplify the explanation, we start with a single projection and later expand to multiple projections from different angles. Let  $\mathbf{P}$  and  $\mathbf{R}$  be the position of the detector and a matrix that rotates from detector coordinates to the global frame, respectively.

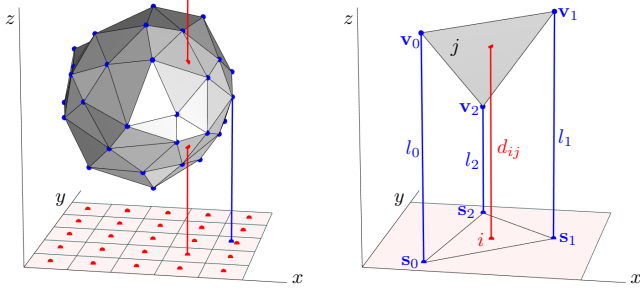


Figure 3: *Left*: The vertices of the triangle mesh (blue dots) are projected onto the detector. Each detector pixel (red dots) is associated with the projection ray which intersects mesh triangles. *Right*: One triangle  $j$ , here given by vertices  $k = 0, 1, 2$ , and one detector pixel  $i$ . Using barycentric coordinates, the distance  $d_{ij}$  may be expressed in terms of  $l_k$ .

If we denote the position of vertex  $k$  in global coordinates by  $\mathbf{V}_k$ , the position in detector coordinates are  $\mathbf{v}_k = \mathbf{R}^\top(\mathbf{V}_k - \mathbf{P})$ . Note that in detector coordinates, the detector itself corresponds to the plane  $z = 0$ , its center is at the origin, and the positive  $z$ -axis points towards the object, see Fig. 3.

Expressed in detector coordinates, the distance of the vertex  $k$  from the detector is trivially  $l_k = \mathbf{z}^\top \mathbf{v}_k$  while  $\mathbf{s}_k = [\mathbf{x} \ \mathbf{y}]^\top \mathbf{v}_k$  are the coordinates of the projection of the vertex onto the detector. Here  $\mathbf{x}$ ,  $\mathbf{y}$ , and  $\mathbf{z}$  are unit vectors in  $x$ ,  $y$  and  $z$  direction, for example  $\mathbf{x} = [1 \ 0 \ 0]^\top$ .

Projecting the object onto the detector pixel  $i$  we consider the projection ray associated with  $i$  (slightly sloppy, call it ray  $i$ ), and its path length in the object. As explained in (Vidal et al., 2009), this can be broken into contribution of all intersections of the ray  $i$  with the mesh triangles

$$p_i = \mu \sum_{j \text{ intersects } i} \text{sign}(\mathbf{z}^\top \mathbf{n}_j) d_{ij} \quad (1)$$

where  $\mathbf{n}_j$  is the normal of the triangle  $j$  (needed for determining the sign of the contribution), and  $d_{ij}$  is the distance of the intersection point to the detector.

Considering now a single triangle  $j$  we express  $d_{ij}$  using barycentric coordinates

$$d_{ij} = \sum_{k \text{ in } j} w_{ij}^k l_k, \quad (2)$$

where  $k$  are the indices of the three vertices of the triangle  $j$  and  $w_{ij}^k$  are the corresponding three barycentric coordinates of pixel  $i$  with respect to the projection of triangle  $j$  onto the detector plane, see Fig. 3, *right*.

To make the forward projection differentiable, we derive

$$\frac{\partial p_i}{\partial \mathbf{v}_k} = \mu \sum_{j \text{ intersects } i} \text{sign}(\mathbf{z}^\top \mathbf{n}_j) \frac{\partial d_{ij}}{\partial \mathbf{v}_k}, \quad (3)$$

and

$$\frac{\partial d_{ij}}{\partial \mathbf{v}_k} = \sum_{k \text{ in } j} \left( w_{ij}^k \frac{\partial l_k}{\partial \mathbf{v}_k} + \frac{\partial w_{ij}^k}{\partial \mathbf{v}_k} l_k \right) = \sum_{k \text{ in } j} \left( [0 \ 0 \ w_{ij}^k] + \frac{\partial w_{ij}^k}{\partial \mathbf{v}_k} l_k \right). \quad (4)$$

For the last step, computation of  $\partial w_{ij}^k / \partial \mathbf{v}_k$ , we employ the idea from (Chen et al., 2019), which reformulates the barycentric form to express the coefficients  $w_{ij}^k$  in terms of 2D projected positions  $\mathbf{s}_k$  and the position of detector pixel  $i$ .

### 3.2. Composite objects

The method described above generalizes to composite objects if certain conditions are met. Specifically, we require that we know beforehand the topology of the parts of the composites, and how parts are embedded within one another. Thus, for each interface triangle we will have a suggestion that what class of material is on either side, but we do not know the specific attenuation coefficient of the classes, since we solve for those.

In order to extend Eq. (1) to composites, we only have to observe that triangles may now be the interface between two materials and not just air and material. This can be handled simply by letting each triangle contribute twice

$$p_i = \sum_j \mu_j \text{sign}(\mathbf{z}^\top \mathbf{n}_j) d_{ij} - \sum_j \bar{\mu}_j \text{sign}(\mathbf{z}^\top \mathbf{n}_j) d_{ij} \quad (5)$$

$$= \sum_j (\mu_j - \bar{\mu}_j) \text{sign}(\mathbf{z}^\top \mathbf{n}_j) d_{ij}, \quad (6)$$

where  $\mu_j$  is the attenuation of the interior material and  $\bar{\mu}_j$  of the exterior material according to normal orientation. Of course, either attenuation will be zero if the material on the corresponding side of the triangle is air.

The derivative of a pixel value with respect to the contributing attenuation  $\mu_m$  for material  $m$  (by abuse of notation) is

$$\frac{\partial p_i}{\partial \mu_m} = \sum_j \pm \text{sign}(\mathbf{z}^\top \mathbf{n}_j) d_{ij}, \quad (7)$$

where the  $\pm$  is positive if the interior material of face  $j$  is labeled as  $m$  and negative if  $m$  is the exterior material. We also modify Eq. (3) by changing  $\mu$  to  $(\mu_j - \bar{\mu}_j)$ .

We have derived the Jacobians in Eq. (3) and (7), which will be used to optimize an objective function  $E$ . That is, we can propagate the gradients from  $E$

$$\frac{\partial E}{\partial \mathbf{v}_k} = \sum_i \frac{\partial E}{\partial p_i} \frac{\partial p_i}{\partial \mathbf{v}_k}, \quad \frac{\partial E}{\partial \mu_m} = \sum_i \frac{\partial E}{\partial p_i} \frac{\partial p_i}{\partial \mu_m}, \quad (8)$$

where the summation is over all the detector pixels.

## 4. Shape from projections

In this section, we use the proposed forward projector to reconstruct shapes from projections. We assume that a template mesh with the correct topology is given. We aim to deform the template mesh and estimate the attenuation coefficients by minimizing the residual between data  $\hat{p}$  and our estimation  $p$ .

Optimizing only the data fitting term can lead to degenerate meshes. To obtain high-quality meshes, we impose three regularization terms. The first term is the Laplacian term (Wang et al., 2018), which constrains the vertices to move similarly with their neighbors, defined by

$$E_{\text{lap}} = \sum_k \|\mathbf{V}_k - \frac{1}{|\mathcal{N}(k)|} \sum_{n \in \mathcal{N}(k)} \mathbf{V}_n\|^2, \quad (9)$$

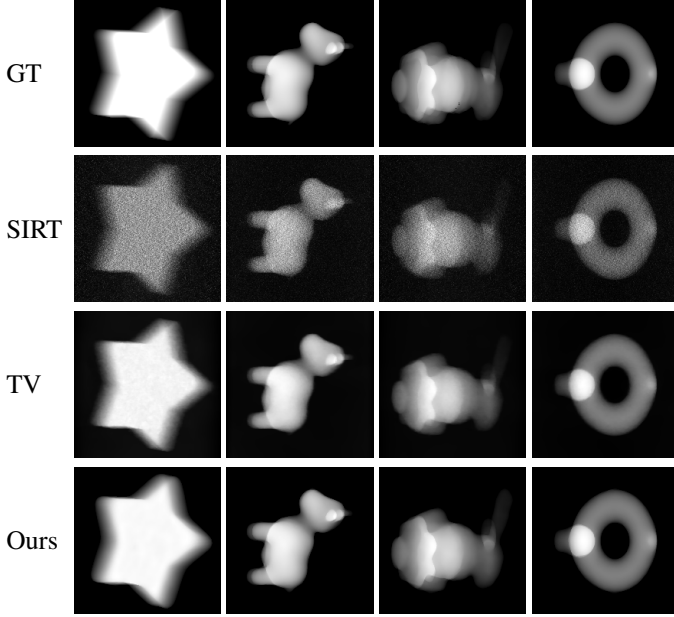


Figure 4: Qualitative results of estimated projections on noisy data with relative noise level 0.4. The first row shows the ground truth, *i.e.*, noise-free data. 2nd-5th row show the forward projection from the solutions by SIRT, TV and the proposed method, respectively.

where  $\mathcal{N}(k)$  is the index set of neighboring vertices to  $k$ -th vertex. The second term is the edge length term to penalize long edges

$$E_{\text{edge}} = \sum_{(\mathbf{V}_k, \mathbf{V}_n) \in G} \|\mathbf{V}_k - \mathbf{V}_n\|^2, \quad (10)$$

where  $G$  denotes the set of edges. Lastly, we impose the flattening term (Kato et al., 2018; Liu et al., 2019)

$$E_{\text{flat}} = \sum_{e \in G} (1 - \cos \theta_e)^2, \quad (11)$$

where  $\theta_e$  is the angle between the normal vectors of two faces sharing the edge  $e$ . Flattening term is needed to remove near-zero volume spikes. These thin artifacts have negligible contribution to the forward projection, and will be ignored by the data fitting term. As shown in Fig. 7, such artifacts can appear during the deformation, but disappear later.

With the data fidelity and regularization terms, the objective function to minimize is

$$E(\{\mathbf{V}_k\}, \{\mu_m\}) = \|p - \hat{p}\|_2^2 + \alpha E_{\text{lap}} + \beta E_{\text{edge}} + \gamma E_{\text{flat}} \quad (12)$$

where  $\alpha, \beta, \gamma$  control the relative weights between the terms. Note that the size of projection data  $\hat{p}$  is the number of detector pixels times the number of projection angles. We use automatic differentiation to minimize  $E$ . For large data, we can use stochastic gradient descent with mini batches in terms of projection angles. In this paper, however, we only consider full batch size of data.

## 5. Experiments and Results

In this section, we present the experimental results of our method on synthetic data of single objects. We also show the

results on real data of a composite object from electron tomography, which has limited range of angles.

### 5.1. Shape reconstruction of watertight objects

*Datasets.* This experiment is designed to test our shape estimation method on noisy simulated data. We use 5 watertight meshes (star, spot, bunny, bob, kitten), shown in the first row of Fig. 5. The attenuation of the objects are set to 1. Generating projections of those meshes using our forward model may resemble to the so-called inverse crime (Mueller and Siltanen, 2012). To avoid it, we employ the Blender software to make projection data based on ray casting methods similar to (Marinovszki et al., 2018). We use 3D parallel projection geometry with 30 projection angles and the detector of size  $192 \times 192$  pixels. The data are shown in the first row of Fig. 4 for one projection view.

*Evaluation metrics.* We compare our result to two standard reconstruction methods: simultaneous iterative reconstruction technique (SIRT) (Andersen and Kak, 1984) and total variation (TV) based reconstruction (Chambolle and Pock, 2011; Sidky et al., 2012). These methods yield 3D images, whereas our method produces surface mesh, making direct comparison of the main output challenging. For consistent comparison, we employ a residual-based metric: *residual projection error* (Roelands et al., 2014), which measures the  $L^2$  norm difference of data and computed projections. We impose the relative Gaussian noise on the original data and calculate the residual projection error between noise-free projections and the estimations of other methods and our method. For SIRT and TV, the reconstruction voxel size is set as  $192 \times 192 \times 192$  and the algorithm parameters are chosen carefully.

*Experimental details.* Our implementation relies on PyTorch (Paszke et al., 2019) and uses Adam (Kingma and Ba, 2015) as an optimizer. The proposed forward projector is implemented as a module in PyTorch. As for the regularization parameters, we fix  $\alpha = 10$ ,  $\gamma = 0.01$  and iterate 500 times. The step size  $\tau$  (learning rate in PyTorch) is set to 0.01 and reduced by half at 400 iteration. During the experiment, we only vary the edge length parameter  $\beta$ . As for initialization, our method begins from an icosphere for genus-0 objects, and from a torus for genus-1 objects. Except for *star* data, we refine the mesh by (Huang et al., 2018) at iteration 60 and improve the mesh quality 3 times by a lightweight repair method (Attene, 2010) at iteration 60, 120, 180. These refine and repair steps help remove artifacts and lead to fast convergence. As also observed in (Vidal et al., 2009), some artifact pixels can appear (e.g., when the ray hits an odd number of times). When a large deformation happens, we may observe some artifact pixels, which we exclude in the objective function. But in the end, we only observe around 2 artifact pixels.

*Robustness to noise.* Our experiments show that the proposed method is robust to noise. Fig. 4 shows projection images of reconstruction results from noisy data with relative noise level 0.4 achieved using SIRT, TV reconstruction and our method. Since SIRT has no regularization it fits closely to the highly noisy

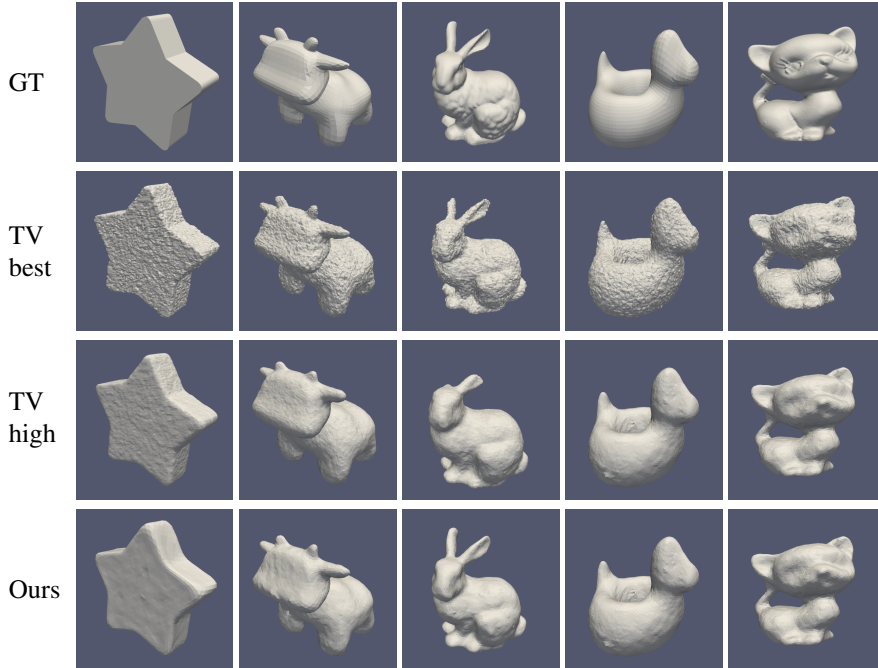


Figure 5: Qualitative results of estimated meshes on noisy data with relative noise level 0.4. The top row shows the ground truth meshes. Rows 2 and 3 show the extracted isosurface from the results of TV reconstruction with the optimal regularization parameter (best) and a high regularization parameter (high), respectively. The last row shows our results.

Table 1: Size of meshes and running times

data	star	spot	bunny	bob	kitten
initial mesh	icosphere (1280 faces)			torus (3200 faces)	
final mesh	no refine.	18680	17908	19308	20904
comp. time	244.1 (sec.)	730.7	719.6	816.3	816.8

data. The results of TV are relatively smooth, but sharp transitions appear blurred. On the other hand, the proposed method yields projections similar to noise-free data. Fig. 5 shows the final mesh results, where the proposed method yields qualitatively better results than TV – we omit highly noisy SIRT results. In Fig. 6 (a), we provide the quantitative results of residual projection error with respect to relative noise levels. Without noise, SIRT gives the superior result as it fits to data without regularization. However, as noise increases, the results of SIRT and TV are shown to be poorer. In (b), we show the effect of edge length parameter on noise-free data. The residual is large for *star* data, due to the coarse resolution of mesh. We observe that if the edge length parameter is less than 1.0, the final meshes might have some artifacts. In Fig. 7. we also show the deformation process of meshes with the corresponding computed projections.

*Computational cost.* Table 1 shows the size of the initial and final mesh and running times. As we do not refine the mesh for *star* object, its computational cost is lower than others. We do the experiment on a Ubuntu server with 256GB RAM and Titan X GPU.

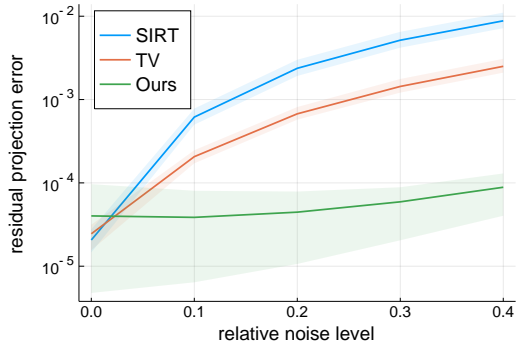
## 5.2. Application to electron tomography

*Datasets.* The goal of this experiment is to estimate the shape of a composite object having Au-core and Ag-shell nano particles and to compute the relative atomic contents between them. We obtain the 2 sets of data of nanorods and nano triangular bipyramid with a similar setting to (Skorikov et al., 2019) except for the tilt ranges (projection angles). The data consist of 49 tilt angles between  $-72^\circ$  to  $72^\circ$ . This limited angle data makes the reconstruction challenging. Fig. 8 (a) shows one projection view of nanorods data and nano triangular bipyramid data. For the nanorods, silica is used outside of the nanorods to fix the shapes during the acquisition.

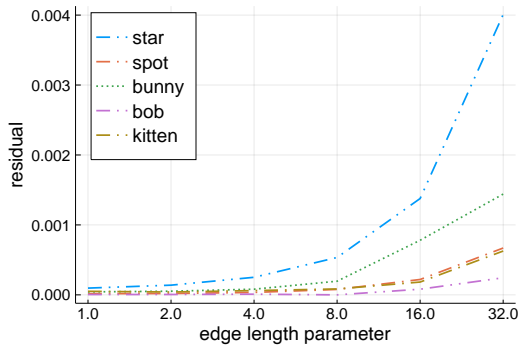
*Evaluation quantity.* To compute the relative atomic contents from our final meshes, we first compute the volumes  $V_{Au}$ ,  $V_{Ag}$  of two output meshes and estimate the number of atoms  $N_{Au}$ ,  $N_{Ag}$ , respectively.<sup>1</sup> Then, the relative atomic content for Au can be computed by  $N_{Au}/(N_{Au} + N_{Ag})$ . To validate the results, we compare our result to (Zanaga et al., 2016) which is based on Energy Dispersive X-ray Spectroscopy (EDXS) in a transmission electron microscopy. EDXS can obtain reliable quantitative chemical information of materials by using the characteristic X-rays (Zanaga et al., 2016). We consider the result of EDXS as the reference to evaluate our results.

*Experimental details.* We initialize the meshes as two icospheres with 160 faces. As the unknown shapes are relatively

<sup>1</sup> $N_{Au} = A_{Au} V_{Au} / M_{Au}$  where  $A_{Au}$  is the bulk density of Au;  $V_{Au}$  its volume; and  $M_{Au}$  its relative atomic mass.



(a) Error bars over 5 datasets



(b) Effect of the regularization parameter  $\beta$

Figure 6: Quantitative results. In (a), the error bars denote the average values with the maximum and minimum value; and the y-axis is in logarithmic scale. (b) shows the residual on noise-free data by our method.

simple, we only impose the Laplacian regularization term with the default value  $\alpha = 10$  for the nanorod data and  $\alpha = 1.0$  for the triangular bipyramid data. We use the collision detection method in (Lauterbach et al., 2009), to make sure that the two nanorodes do not collide. In this experiment, we set the step size  $\tau = 0.005$  and observe no collisions.

Table 2: Estimated atomic percentage for Au

Method	nanorod	triangular bipyramid
EDXS (Reference)	58.73 %	7.25 %
(Skorikov et al., 2019)	59.80 %	<b>7.06 %</b>
Ours	<b>59.36 %</b>	7.51 %

*Results.* Fig. 8 (c) shows our final estimated 3D shapes from (b) the two icospheres. Table 2 provides the quantitative results of the atomic percentage for Au. The results of both ours and voxel-based method (Skorikov et al., 2019) are close to the reference result by EDXS. An advantage of our method is that our method directly solves shapes without a post-processing, whereas (Skorikov et al., 2019) needs a post processing such as applying morphological operators, after image reconstruction.

## 6. Discussion and conclusion

Compared with other reconstruction methods, our approach has advantages when reconstructing homogeneous objects with

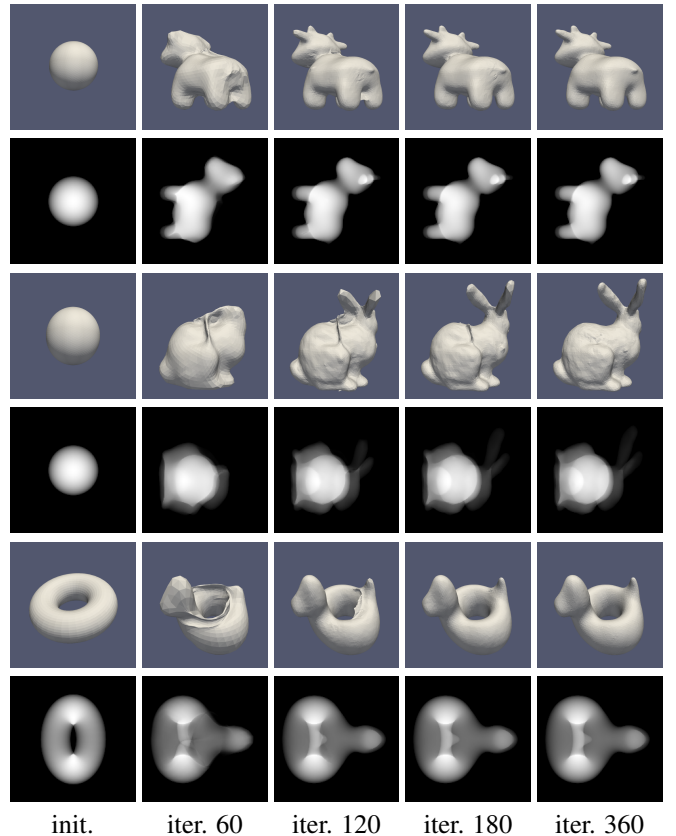


Figure 7: Deformation examples. The odd rows show the intermediate meshes during deformation and the even rows show the corresponding computed projections for one projection angle. We refine the mesh in finer resolution at iteration 60 and fix the mesh at iterations 120 and 180.

relatively simple geometry, and when the data foundation is noisy or limited. Here, we explained our method in parallel geometry where rays are perpendicular to the detector plane, but it may be extended to a more general setting such as cone beam geometry (Buzug, 2008).

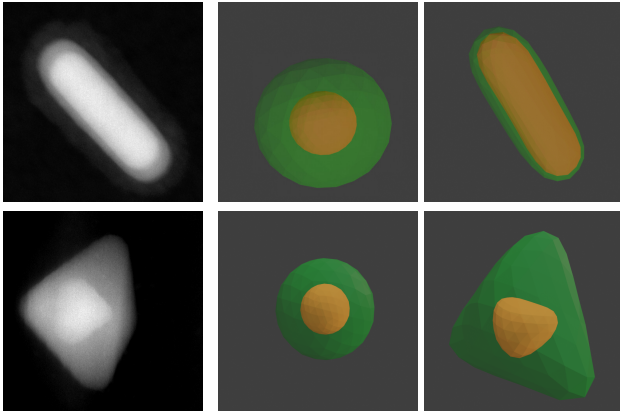
As a potential application, our method can be useful for estimating the geometry precisely, e.g., to register the reconstructed object to the 3D CAD model. Another application can be dynamic tomography where we aim to analyze the objects which are changed during scanning. From an initial configuration of the object, the proposed method can estimate the displacement between time steps more efficiently than voxel-based methods.

## Acknowledgments

This work is funded by EU Horizon 2020 MSCA Innovative Training Network MUMMERING Grant Number 765604.

## References

- Aghasi, A., Kilmer, M., Miller, E.L., 2011. Parametric Level Set Methods for Inverse Problems. *SIAM J. Imaging Sci.* 4.
- Alvino, C.V., Yezzi, A.J., 2004. Tomographic reconstruction of piecewise smooth images, in: *IEEE Conference on Computer Vision and Pattern Recognition.*



(a) One view of data (b) Initialization (c) final 3D shapes

Figure 8: Projection data and rendering of our results for nano rod (top) and nano triangular bipyramid (bottom). In both cases, the meshes are initialized as the same composite spheres but rendered with different settings for the illustration purpose.

- Andersen, A.H., Kak, A.C., 1984. Simultaneous Algebraic Reconstruction Technique (SART): A superior implementation of the ART algorithm. *Ultrason. Imaging* 6.
- Attene, M., 2010. A lightweight approach to repairing digitized polygon meshes. *Vis. Comput.* 26.
- Aveyard, R., Zhong, Z., Batenburg, K.J., Rieger, B., 2017. Optimizing experimental parameters for the projection requirement in HAADF-STEM tomography. *Ultramicroscopy* 177.
- Bonin, A., Chalmond, B., Lavayssière, B., 2002. Monte-Carlo simulation of industrial radiography images and experimental designs. *NDT & E International* 35.
- Buzug, T.M., 2008. *Computed Tomography from Photon Statistics to Modern Cone Beam CT*. Springer.
- Chambolle, A., Pock, T., 2011. A First-Order Primal-Dual Algorithm for Convex Problems with Applications to Imaging. *J. Math. Imaging Vis.* 40.
- Chen, W., Gao, J., Ling, H., Smith, E.J., Lehtinen, J., Jacobson, A., Fidler, S., 2019. Learning to Predict 3D Objects with an Interpolation-based Differentiable Renderer, in: *Neural Information Processing Systems*.
- Dahl, V.A., Dahl, A.B., Hansen, P.C., 2018. Computing segmentations directly from x-ray projection data via parametric deformable curves. *Meas. Sci. Technol.* 29.
- Elangovan, V., Whitaker, R.T., 2001. From Sinograms to Surfaces: A Direct Approach to the Segmentation of Tomographic Data, in: *Medical Image Computing and Computer-Assisted Intervention (MICCAI)*.
- Eliasof, M., Sharf, A., Treister, E., 2020. Multi-modal 3D shape reconstruction under calibration uncertainty using parametric level set methods. *SIAM J. Imaging Sci.* 13.
- Freud, N., Duvauchelle, P., Létang, J.M., Babot, D., 2006. Fast and robust ray casting algorithms for virtual X-ray imaging. *Nuclear Instruments and Methods in Physics Research Section B: Beam Interactions with Materials and Atoms* 248.
- Gadella, M., Wang, R., Maji, S., 2019. Shape Reconstruction Using Differentiable Projections and Deep Priors, in: *International Conference on Computer Vision*.
- Huang, J., Su, H., Guibas, L., 2018. Robust Watertight Manifold Surface Generation Method for ShapeNet Models. *ArXiv180201698 Cs*.
- Kadu, A., van Leeuwen, T., Batenburg, K.J., 2018. A parametric level-set method for partially discrete tomography, in: *International Conference on Discrete Geometry for Computer Imagery*.
- Kass, M., Witkin, A., Terzopoulos, D., 1988. Snakes: Active contour models. *Int. J. Comput. Vis.* 1.
- Kato, H., Ushiku, Y., Harada, T., 2018. Neural 3D Mesh Renderer, in: *IEEE Conference on Computer Vision and Pattern Recognition*.
- Kingma, D., Ba, J., 2015. Adam: A method for stochastic optimization, in: *International Conference on Learning Representations*.
- Lauterbach, C., Garland, M., Sengupta, S., Luebke, D.P., Manocha, D., 2009. Fast BVH Construction on GPUs. *Comput. Graph. Forum* 28.
- Liu, S., Chen, W., Li, T., Li, H., 2019. Soft Rasterizer: Differentiable Rendering for Unsupervised Single-View Mesh Reconstruction, in: *International Conference on Computer Vision*.
- Loper, M.M., Black, M.J., 2014. OpenDR: An Approximate Differentiable Renderer, in: *European Conference on Computer Vision*.
- Marinovszki, Á., Beenhouwer, J.D., Sijbers, J., 2018. An efficient CAD projector for X-ray projection based 3D inspection with the ASTRA Toolbox, in: *Conference on Industrial Computed Tomography*.
- Midgley, P.A., Dunin-Borkowski, R.E., 2009. Electron tomography and holography in materials science. *Nat. Mater.* 8.
- Mueller, J.L., Siltanen, S., 2012. *Linear and Nonlinear Inverse Problems with Practical Applications*. volume 10. Society for Industrial and Applied Mathematics.
- Mumford, D., Shah, J., 1989. Optimal approximations by piecewise smooth functions and associated variational problems. *Commun. Pure Appl. Math.* 42.
- Osher, S., Fedkiw, R., 2004. Level set methods and dynamic implicit surfaces. *Appl. Mech. Rev.* 57.
- Paszke, A., Gross, S., Massa, F., Lerer, A., Bradbury, J., Chanan, G., Killeen, T., Lin, Z., Gimelshein, N., Antiga, L., Desmaison, A., Köpf, A., Yang, E., DeVito, Z., Raison, M., Tejani, A., Chilamkurthy, S., Steiner, B., Fang, L., Bai, J., Chintala, S., 2019. PyTorch: An imperative style, high-performance deep learning library, in: *Neural Information Processing Systems*.
- Roelands, T., Batenburg, K.J., den Dekker, A.J., Sijbers, J., 2014. The reconstructed residual error: A novel segmentation evaluation measure for reconstructed images in tomography. *Comput. Vis. Image Underst.* 126.
- Sidky, E.Y., Jørgensen, J.H., Pan, X., 2012. Convex optimization problem prototyping for image reconstruction in computed tomography with the Chambolle–Pock algorithm. *Phys. Med. Biol.* 57.

- Skorikov, A., Albrecht, W., Bladt, E., Xie, X., van der Hoeven, J.E.S., van Blaaderen, A., Van Aert, S., Bals, S., 2019. Quantitative 3D Characterization of Elemental Diffusion Dynamics in Individual Ag@Au Nanoparticles with Different Shapes. *ACS Nano* 13.
- Sujar, A., Meuleman, A., Villard, P.F., Garcia, M., Vidal, F., 2017. gVirtualXRay: Virtual x-ray imaging library on GPU, in: *Computer Graphics and Visual Computing (CGVC)*.
- Vidal, F.P., Garnier, M., Freud, N., Létang, J.M., John, N.W., 2009. Simulation of X-ray attenuation on the GPU, in: *Proceedings of Theory and Practice of Computer Graphics*, Eurographics Association, Cardiff, UK.
- Wang, N., Zhang, Y., Li, Z., Fu, Y., Liu, W., Jiang, Y.G., 2018. Pixel2Mesh: Generating 3D Mesh Models from Single RGB Images, in: *European Conference on Computer Vision*.
- Whitaker, R.T., Elangovan, V., 2002. A direct approach to estimating surfaces in tomographic data. *Med. Image Anal.* 6.
- Zanaga, D., Altantzis, T., Sanctorem, J., Freitag, B., Bals, S., 2016. An alternative approach for  $\zeta$ -factor measurement using pure element nanoparticles. *Ultramicroscopy* 164.